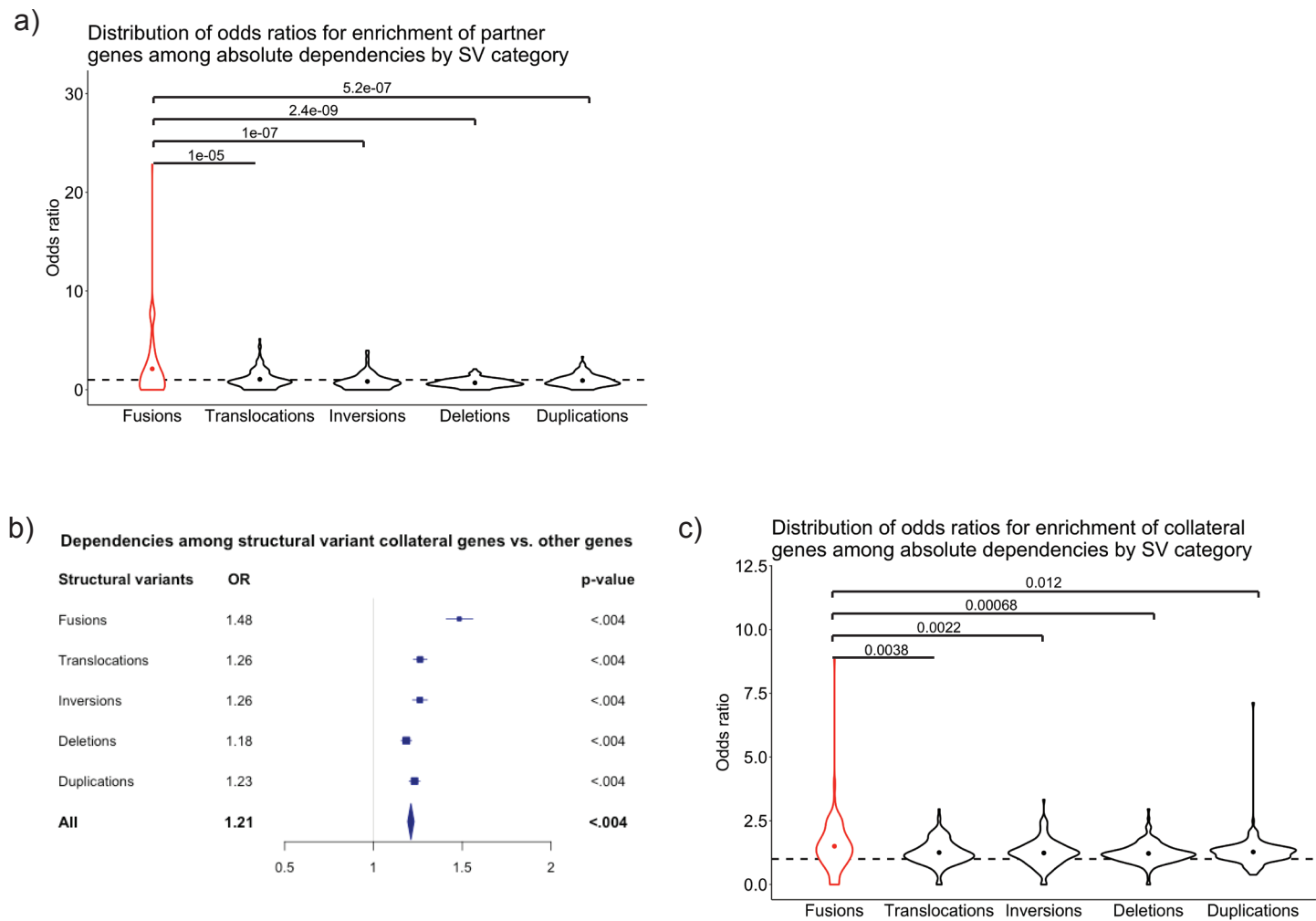
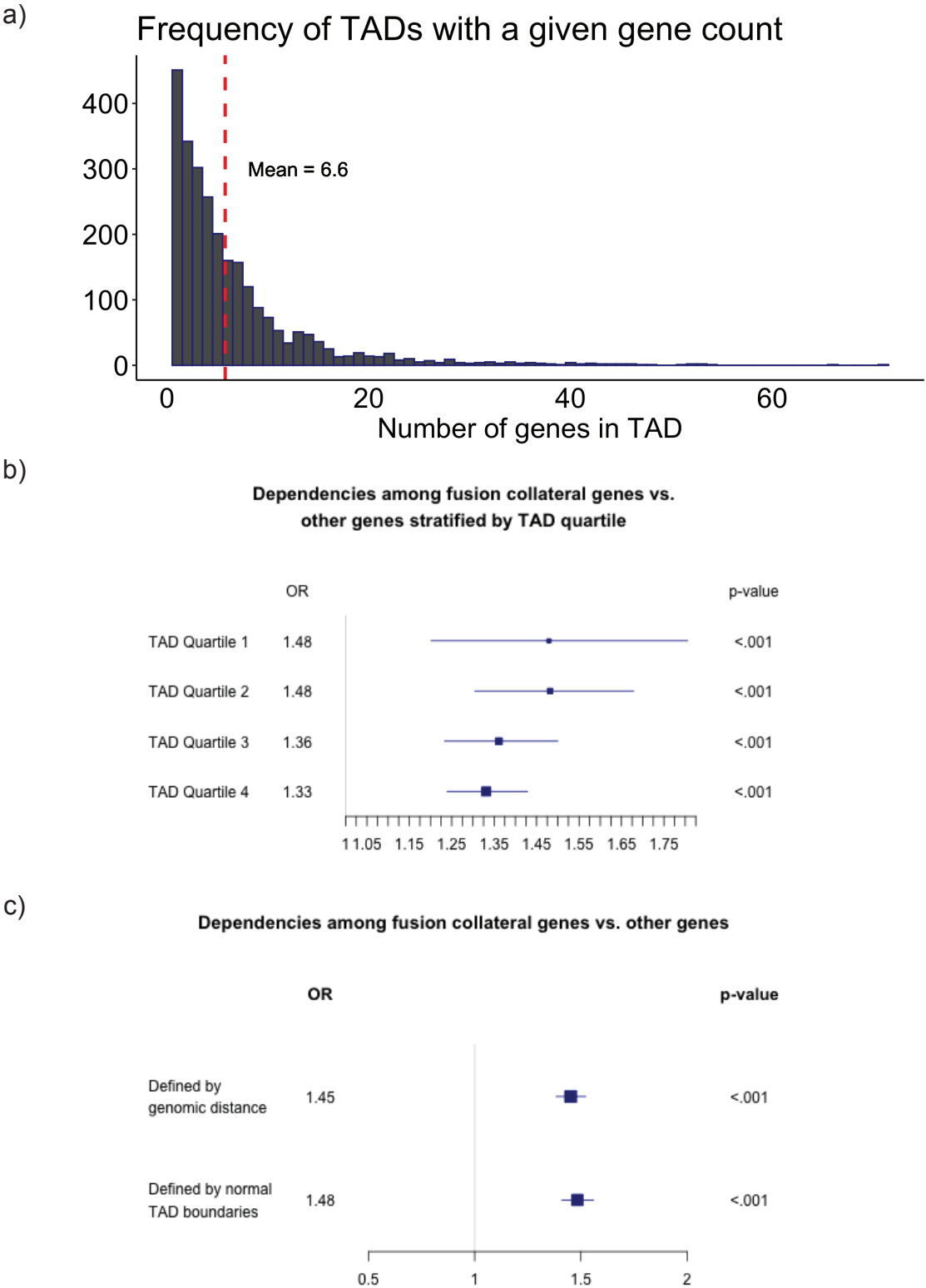


Supplementary Figure 1



Supplementary Figure 1: Enrichment analyses of partner and collateral genes among absolute dependencies across SV categories. **a**, Distribution of ORs among individual cell lines for enrichment of partner genes among absolute dependencies (dashed line OR = 1, p-values calculated by two-sided t-test). **b**, Aggregate ORs and p-values for enrichment of collateral genes among absolute dependencies, stratified by category of structural variant (Fisher's exact test, FWER < .05 to ascertain significance, using a Bonferroni correction for the hypotheses tested results in a threshold of p < .004 to ascertain significant associations). **c**, Distribution of ORs among individual cell lines for enrichment of collateral genes among absolute dependencies (dashed line OR = 1, p-values calculated by two-sided t-test).

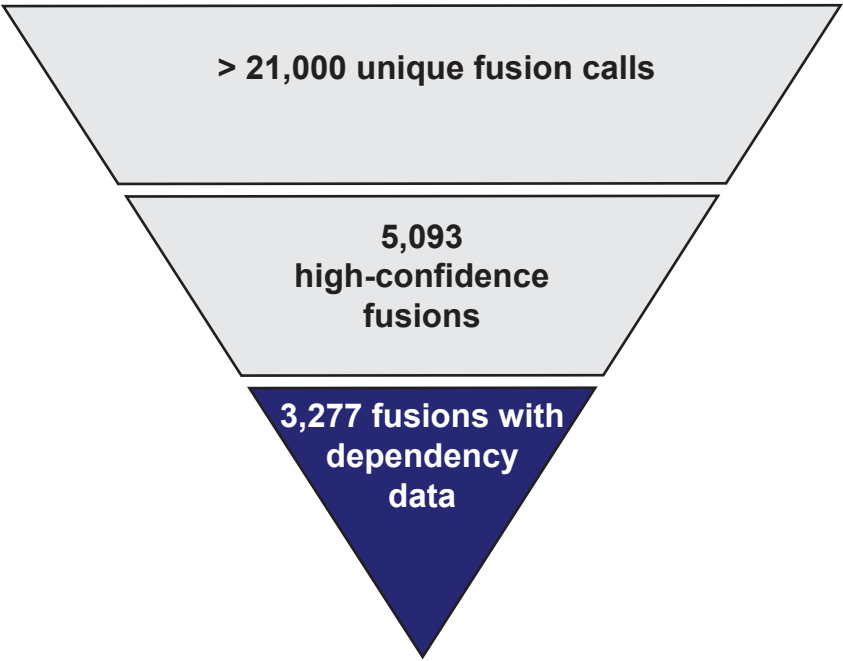
Supplementary Figure 2



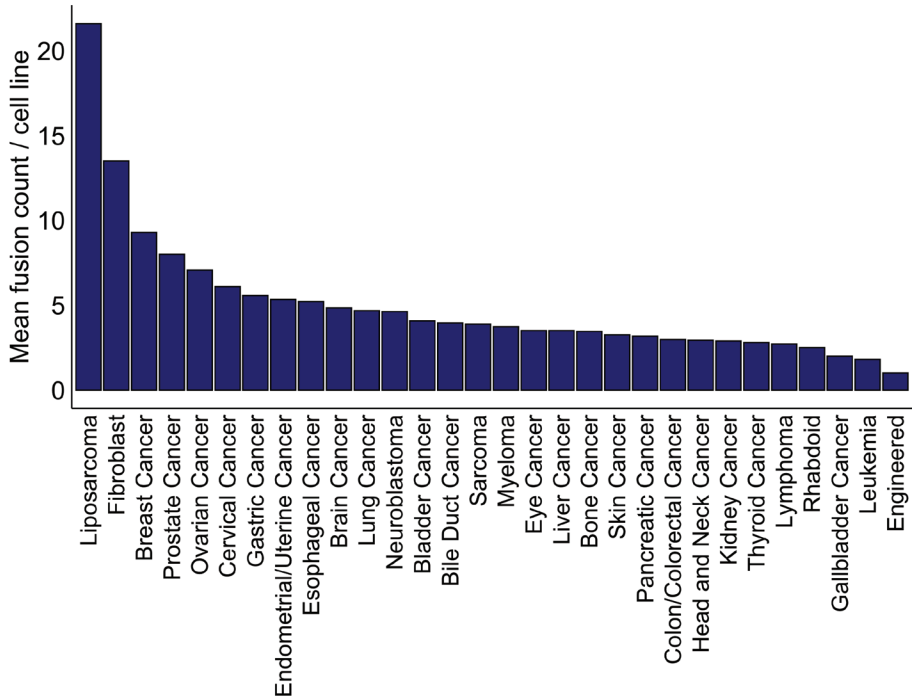
Supplementary Figure 2: Implications of TAD boundary definitions and size. **a**, Distribution of gene counts in TAD definitions utilized in this study. TADs with at least one protein-coding gene range from having 1-71 genes attributed to them, with a mean of ~6 genes per TAD. **b**, Stratifying enrichment analysis for collateral genes among dependencies in the context of fusions. Fusion collateral genes remain enriched among absolute dependencies regardless of TAD size ($p < .001$ by Fisher's exact tests). **c**, Modified enrichment analysis for fusion collateral genes among dependencies utilizing standardized symmetric genomic window of 930 kb compared to TAD boundaries used in current study. The enrichment of collateral genes amongst dependencies in the context of fusions is comparable between both scenarios ($p < .001$ by Fisher's exact tests).

Supplementary Figure 3

a)

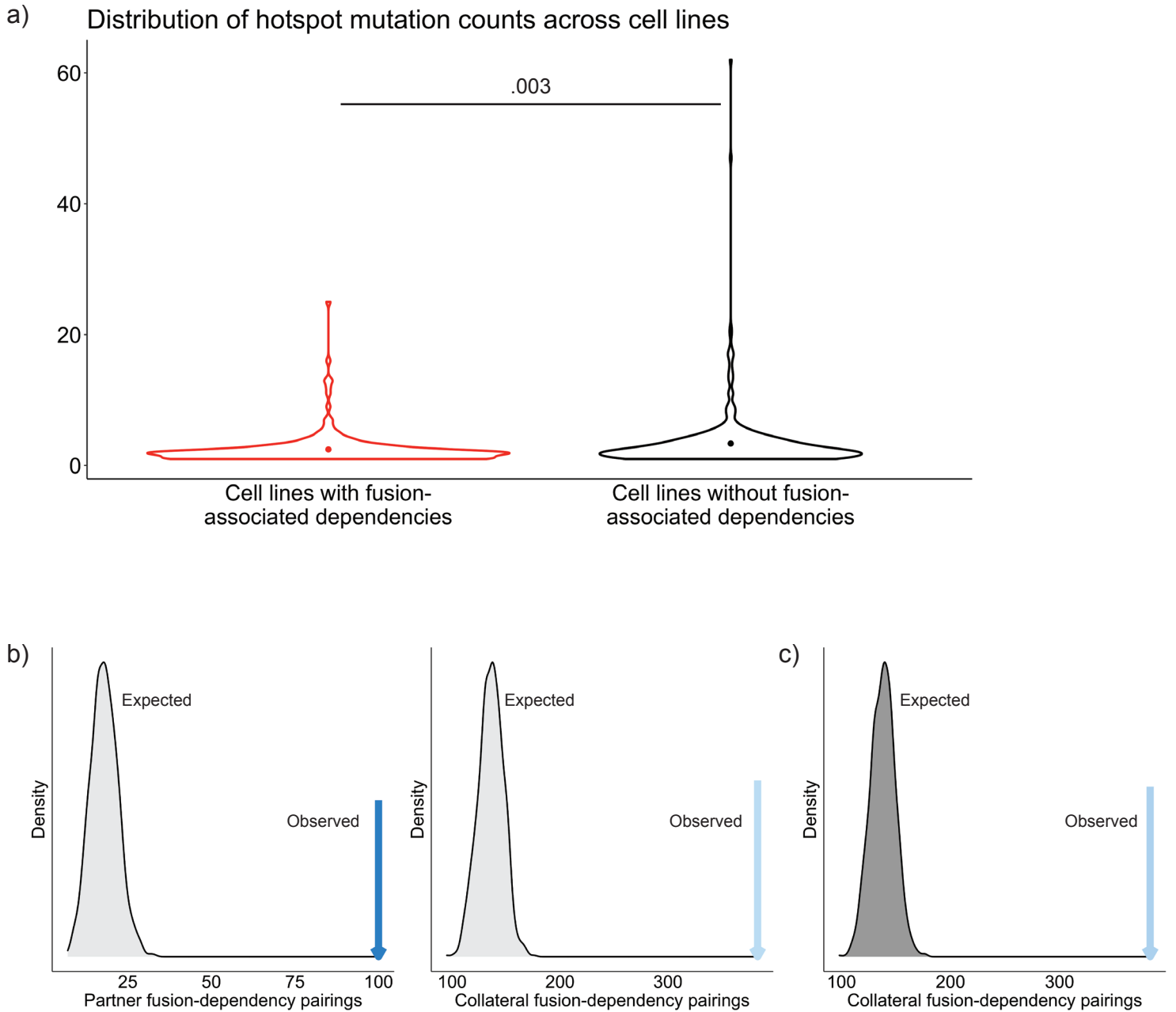


b)

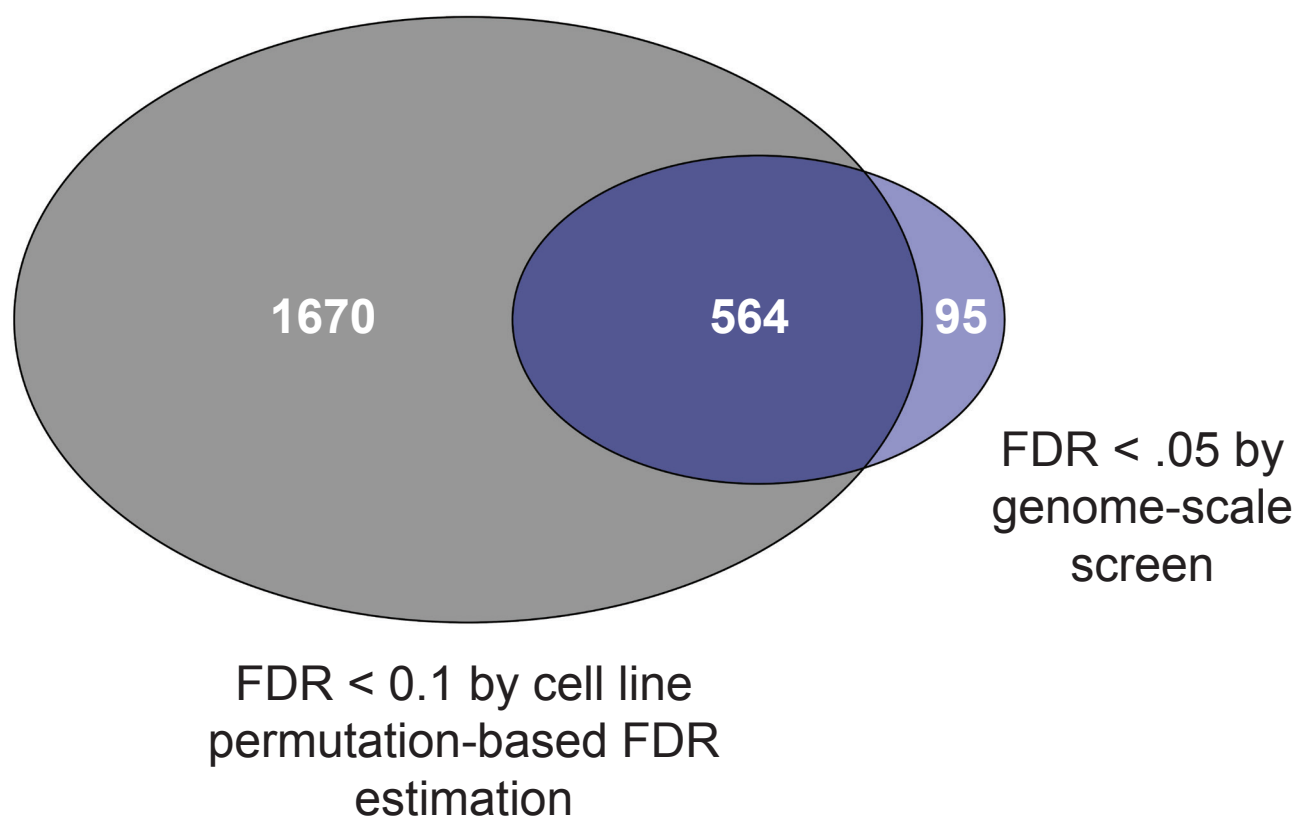


Supplementary Figure 3: Summary of fusion calls. **a**, Filtering fusion calls across the Cancer Cell Line Encyclopedia (CCLE) to arrive at the final set used to explore associated dependencies. **b**, Disease types rank-ordered by average number of fusions detected per cell line.

Supplementary Figure 4

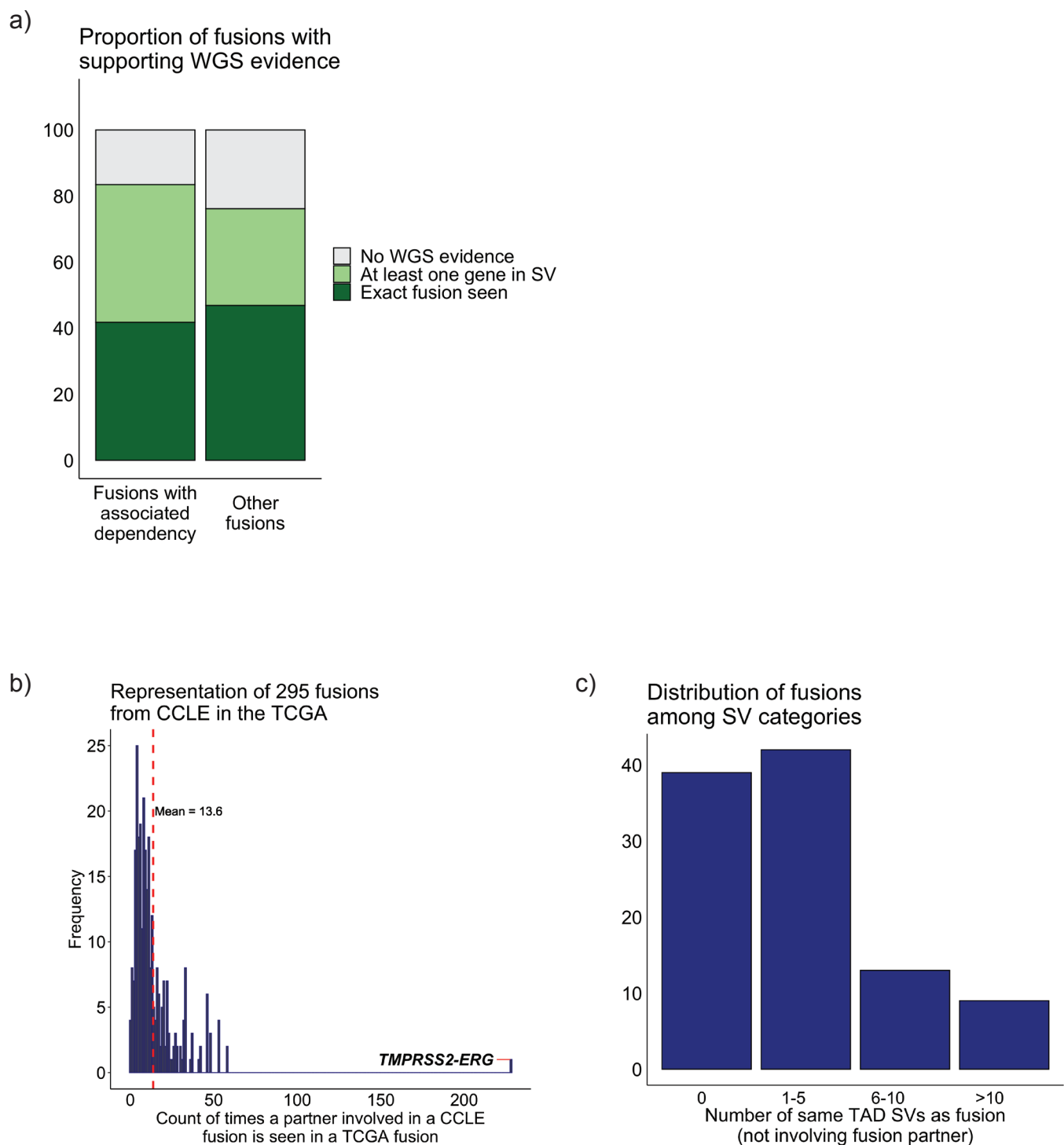


Supplementary Figure 4: Distribution of hotspot mutation counts in the presence/ absence of fusion-associated dependencies; Gene-label permutation testing to compare expected vs. observed frequencies of fusion-associated dependencies. **a**, In evaluating cell lines with at least one hotspot driver mutation, cell lines with fusion-associated dependencies had significantly fewer hotspot driver mutations when compared to cell lines without fusion-associated dependencies (point represents mean of each distribution, p-value calculated by two-sided t-test). **b**, Observed conservative count of total fusion-dependency pairings compared to the null distribution of expected fusion-dependency pairings obtained by 1,000 gene-label permutations for each of 3,277 fusion-dependency relationships. Left: Partner fusion-dependency pairings ($p < .001$). Right: Collateral fusion-dependency pairings ($p < .001$). **c**, Updated null model for collateral fusion-dependency pairings derived from gene-label permutations controlling for TAD size. There is no significant change in the null model, and observed conservative count of collateral fusion-dependency pairings is still significantly greater than what would be expected by chance ($p < .001$).



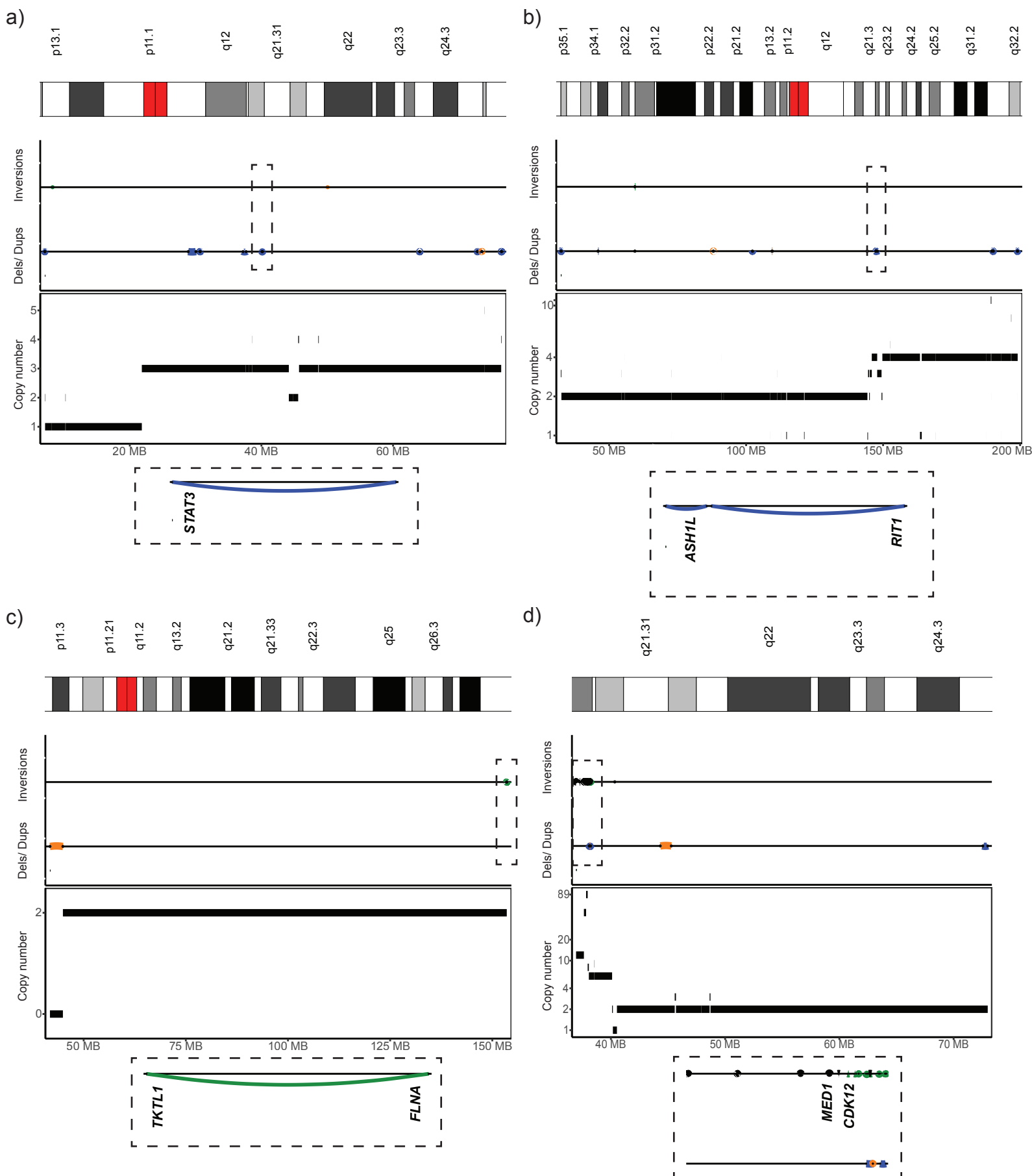
Supplementary Figure 5: Comparison of fusion-dependency pairings identified by cell line permutation-based FDR estimation (with FDR < 0.1) and genome-scale screen. Comparison of fusion-dependency pairings identified by cell line permutation-based FDR estimation (grey) and genome-scale screen (blue).

Supplementary Figure 6



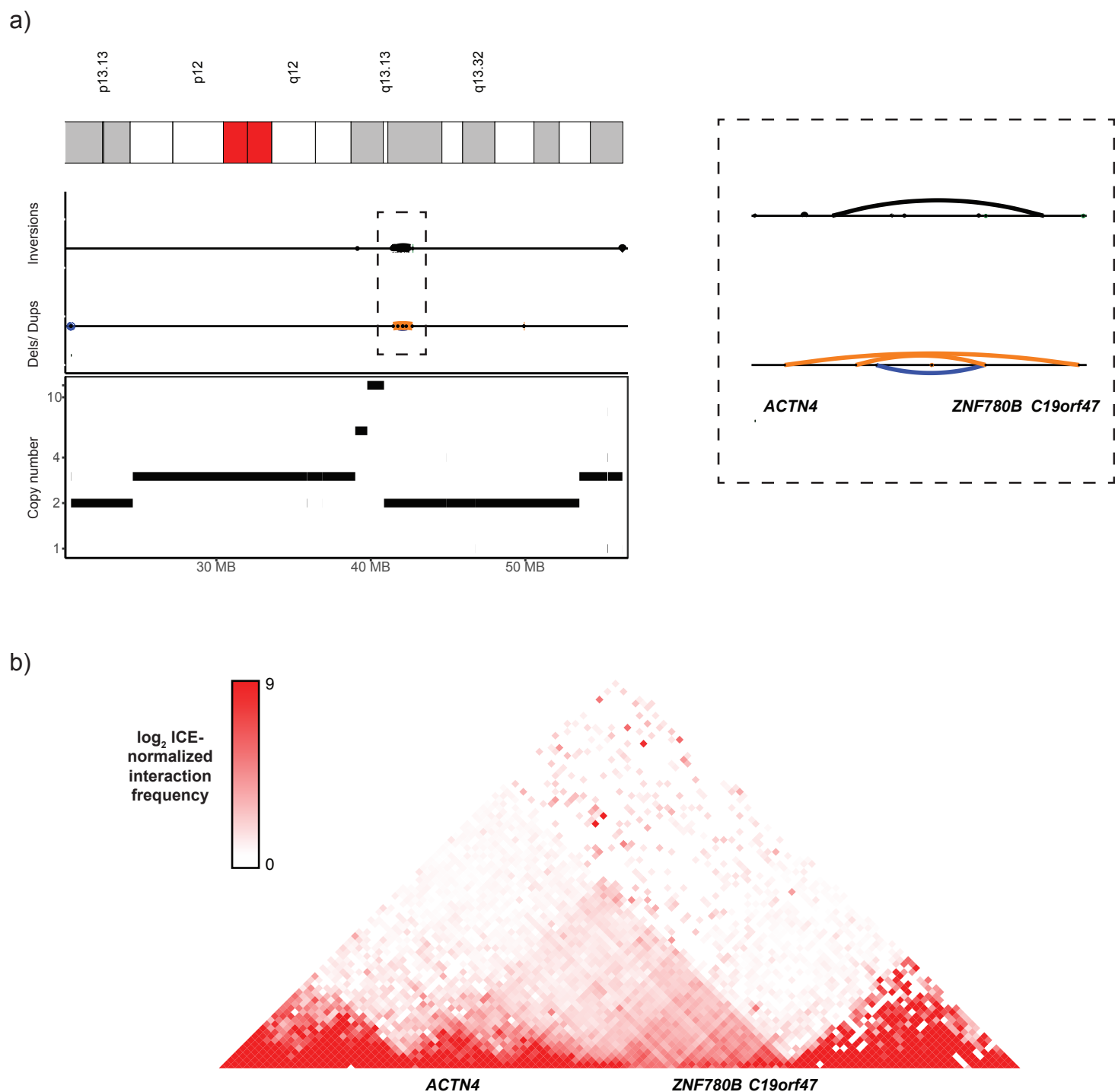
Supplementary Figure 6: Supporting WGS data for the existence of fusions; CCLE fusion representation in the TCGA; and same TAD SVs. a, Total counts reflect fusion-cell contexts (e.g., the same fusion in multiple different cells is evaluated independently for the presence of supporting WGS data). **b,** Representation of 295 fusions from the CCLE in the TCGA. Fusions identified as having associated dependencies in the CCLE have partners that are recurrently seen among TCGA fusions. **c,** Count of fusions with associated dependencies grouped by number of same TAD SVs identified.

Supplementary Figure 7



Supplementary Figure 7: Synthesis of copy number and structural variant data for fusions with associated dependencies in different cell lines. Legend: black = head-to-head inversion, green = tail-to-tail inversion, orange = deletion, blue = duplication. Simple structural variants associated with **a**, STAT3-CAVIN1 fusion on Chromosome 17 in breast cancer cell line HCC38 **b**, ASH1L-RIT1 fusion on chromosome 1 in breast cancer cell line DU4475, **c**, and TKTL1-FLNA fusion on chromosome X in AML cell line THP1. **d**, Multiple SVs in close proximity to the MED1-CDK12 fusion on chromosome 17 in gastric cancer cell line NCIN87.

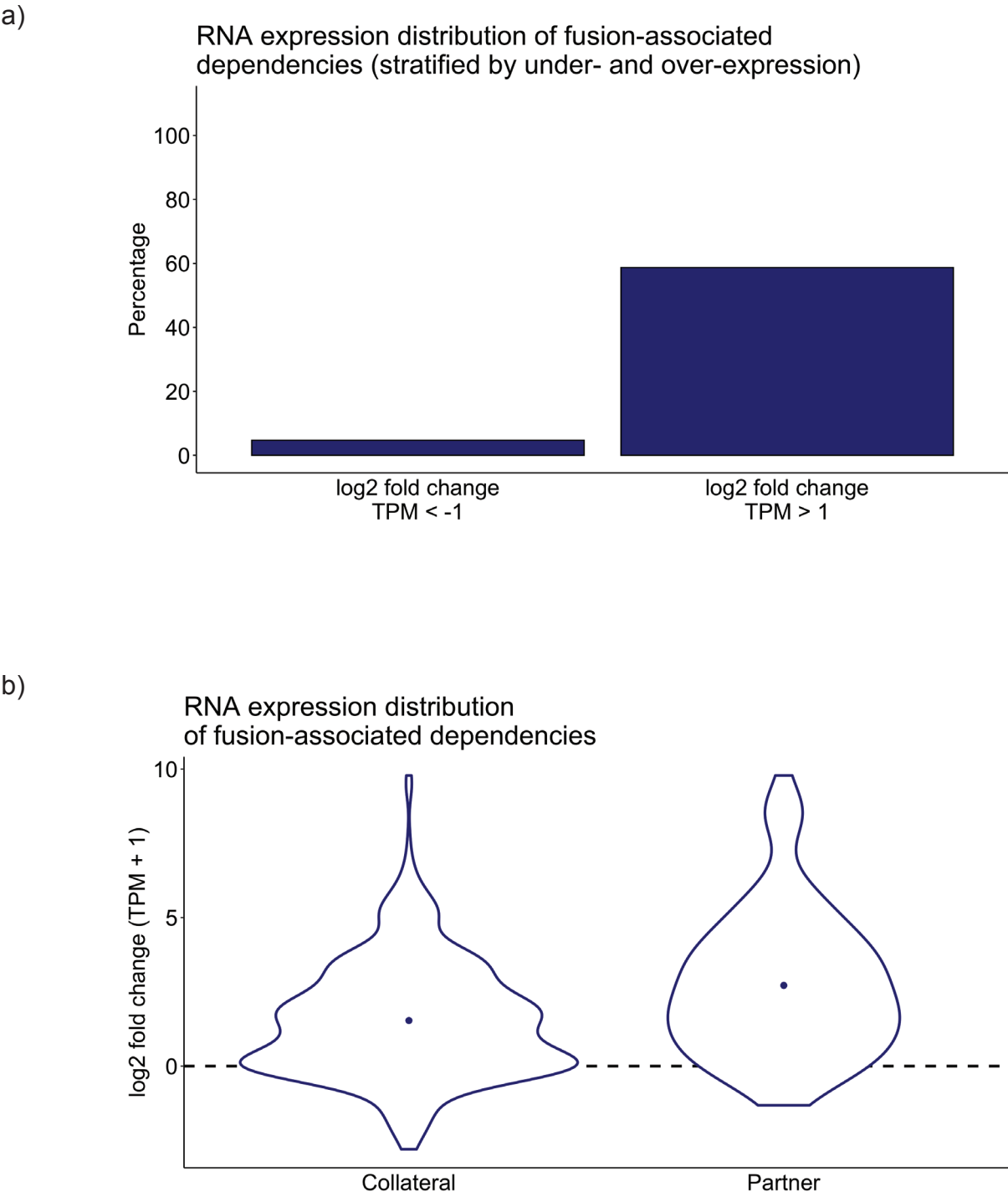
Supplementary Figure 8



Supplementary Figure 8: Fusion-associated dependency on chromosome 19 in pancreatic cancer cell line PANC1.

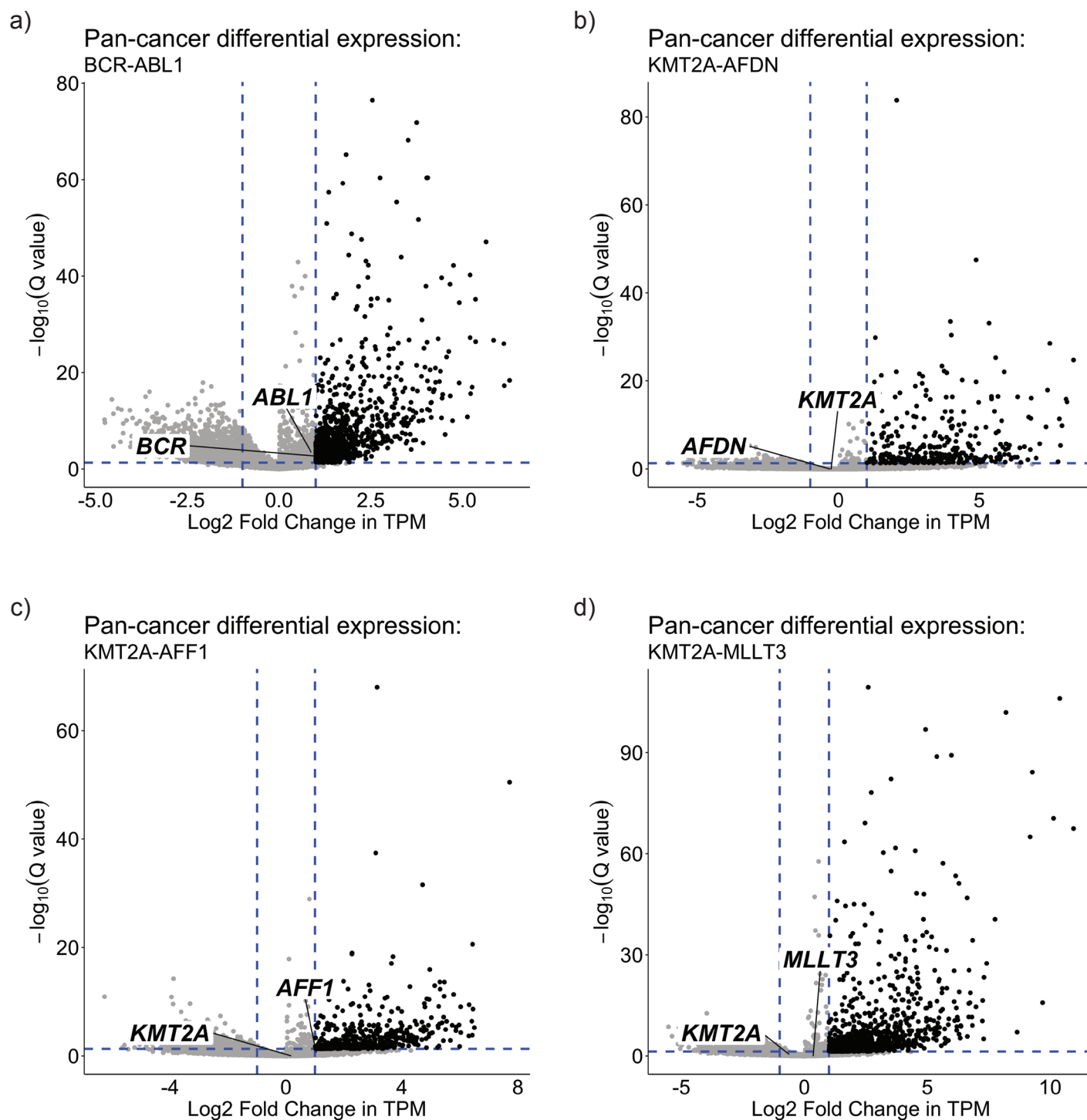
Legend: black = head-to-head inversion, green = tail-to-tail inversion, orange = deletion, blue = duplication. **a**, There are multiple localized structural variants near the identified collateral dependency ZNF780B, including a deletion involving ACTN4 and C19orf47, as well as an inversion involving C19orf47. **b**, Interaction frequencies for region of chromosome 19 in PANC1 with ACTN4-C19orf47 fusion and collateral dependency ZNF780B.

Supplementary Figure 9



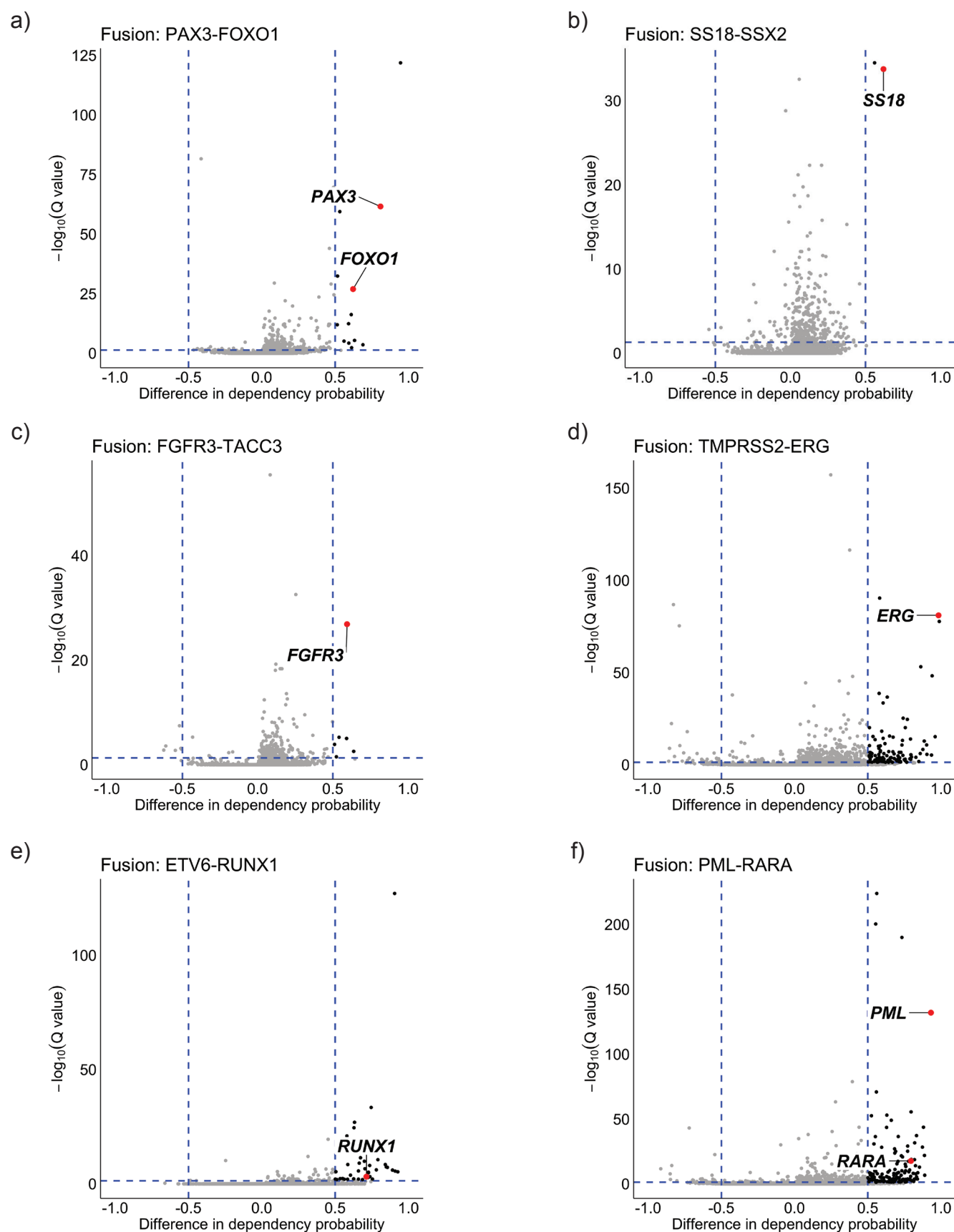
Supplementary Figure 9: RNA expression distribution of fusion-associated dependencies. **a**, Stratified by under- and over-expression relative to mean expression across DepMap. Significantly more fusion-dependency pairings are overexpressed than underexpressed ($p < .001$, Fisher's exact test). **b**, Distribution of log2-fold-change RNA expression of fusion-associated dependencies relative to DepMap mean expression. Both partner (mean log2-fold-change 2.7) and collateral (mean log2-fold-change 1.5) fusion-associated dependencies are associated with RNA overexpression.

Supplementary Figure 10



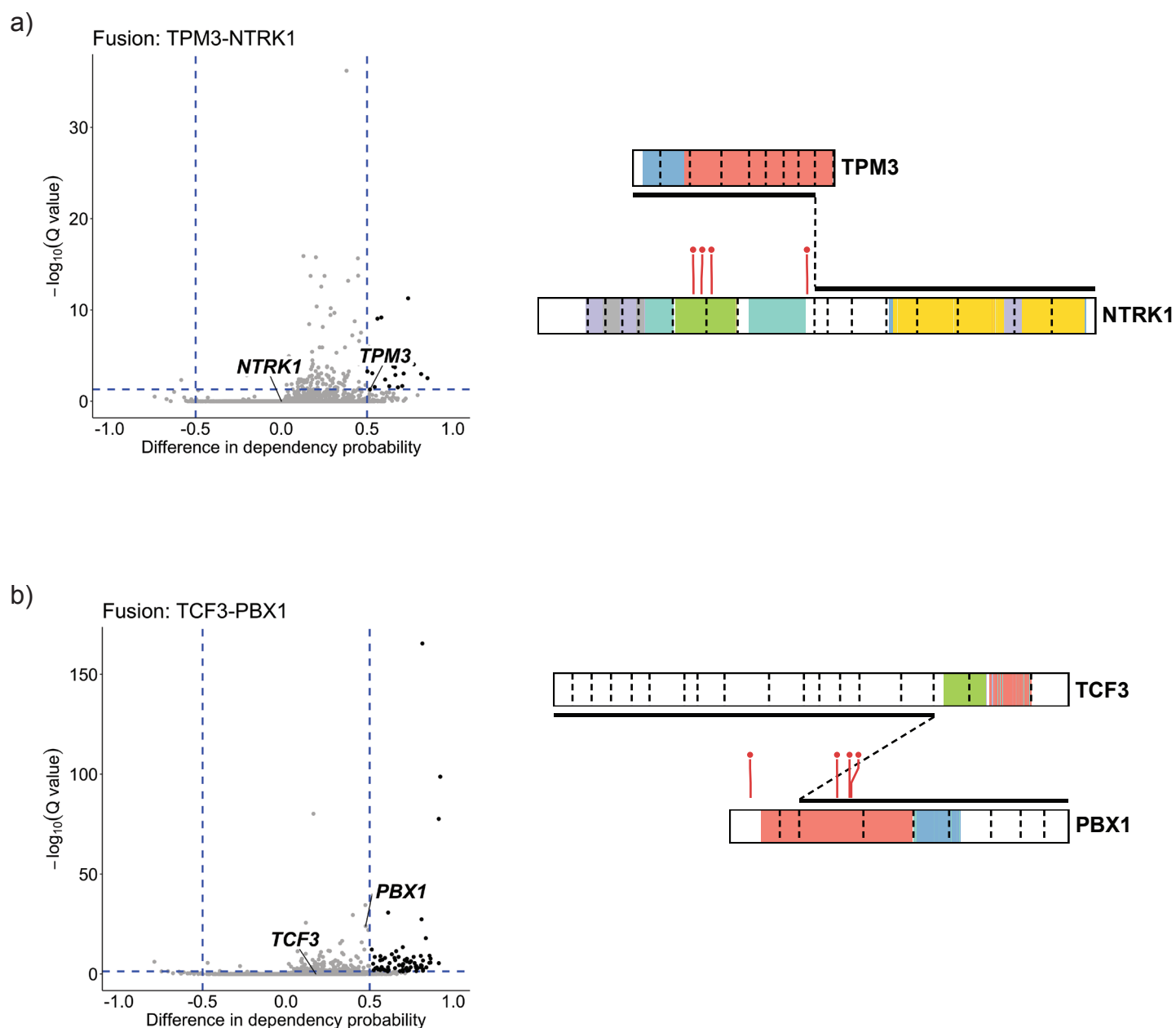
Supplementary Figure 10: Differential RNA expression for BCR-ABL1 and KMT2A fusions. **a**, Unbiased differential expression space for BCR-ABL1 in 16 cell lines. **b**, Unbiased differential expression space for KMT2A-AFDN in 2 cell lines. **c**, Unbiased differential expression space for KMT2A-AFF1 in 4 cell lines. **d**, Unbiased differential expression space for KMT2A-MLLT3 in 5 cell lines.

Supplementary Figure 11



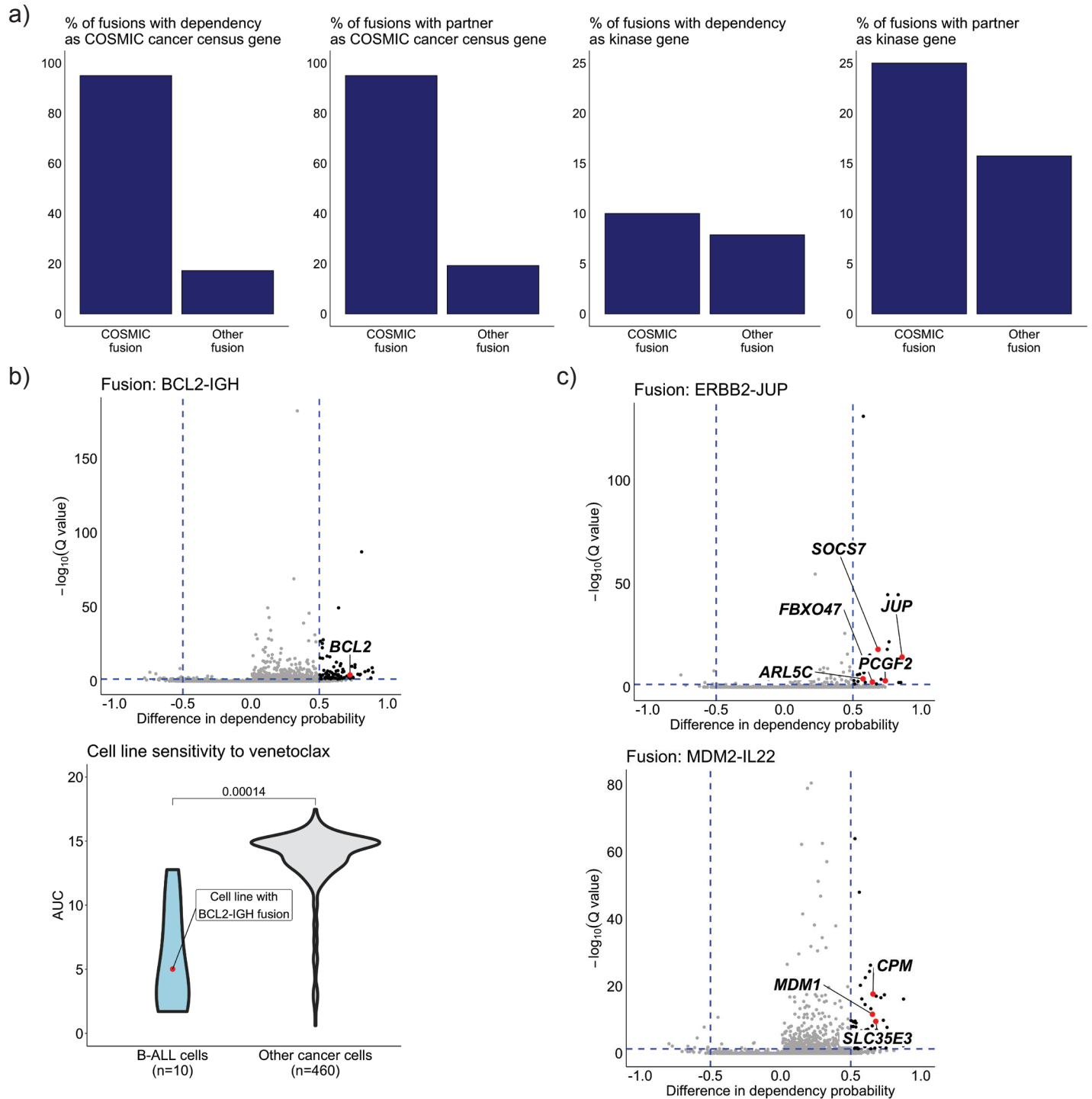
Supplementary Figure 11: Other COSMIC fusions with associated dependencies. a, PAX3-FOXO1. b, SS18-SSX2. c, FGFR3-TACC3. d, TMPRSS2-ERG. e, ETV6-RUNX1. f, PML-RARA.

Supplementary Figure 12



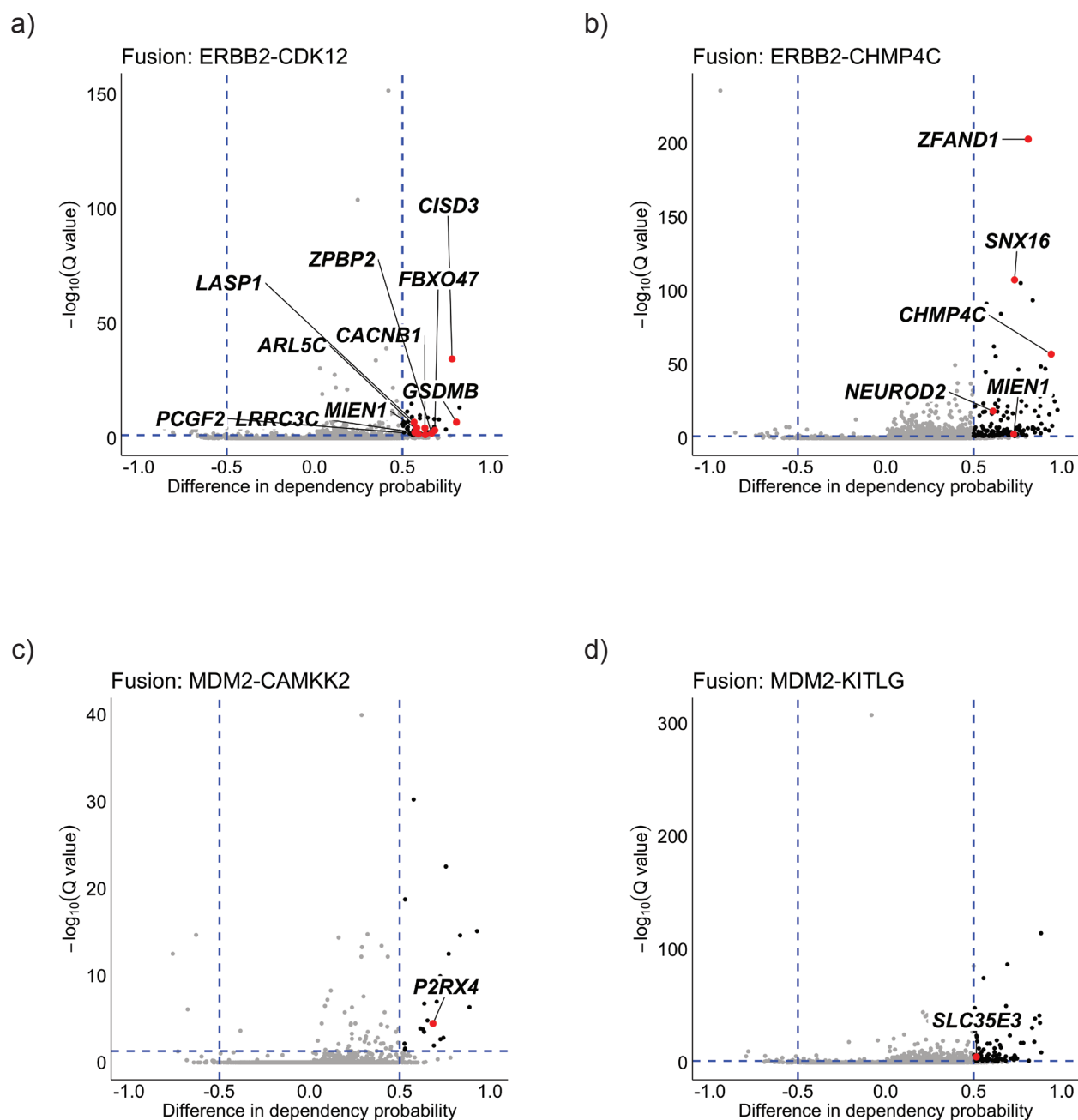
Supplementary Figure 12: COSMIC fusions without fusion-associated dependencies. **a**, Dependency space for cell line with TPM3-NTRK1 fusion. NTRK1 does not screen as a dependency because of sgRNA location (red lines) on the TPM3-NTRK1 fusion transcript, with breakpoint illustrated. Colored regions represent known functional domains. **b**, Dependency space for cell line with TCF3-PBX1 fusion. PBX1 does not screen as a dependency despite sgRNA location (red lines) on the TCF3-PBX1 fusion transcript, as differential dependency probability score does not reach threshold of 50%. Colored regions represent known functional domains.

Supplementary Figure 13



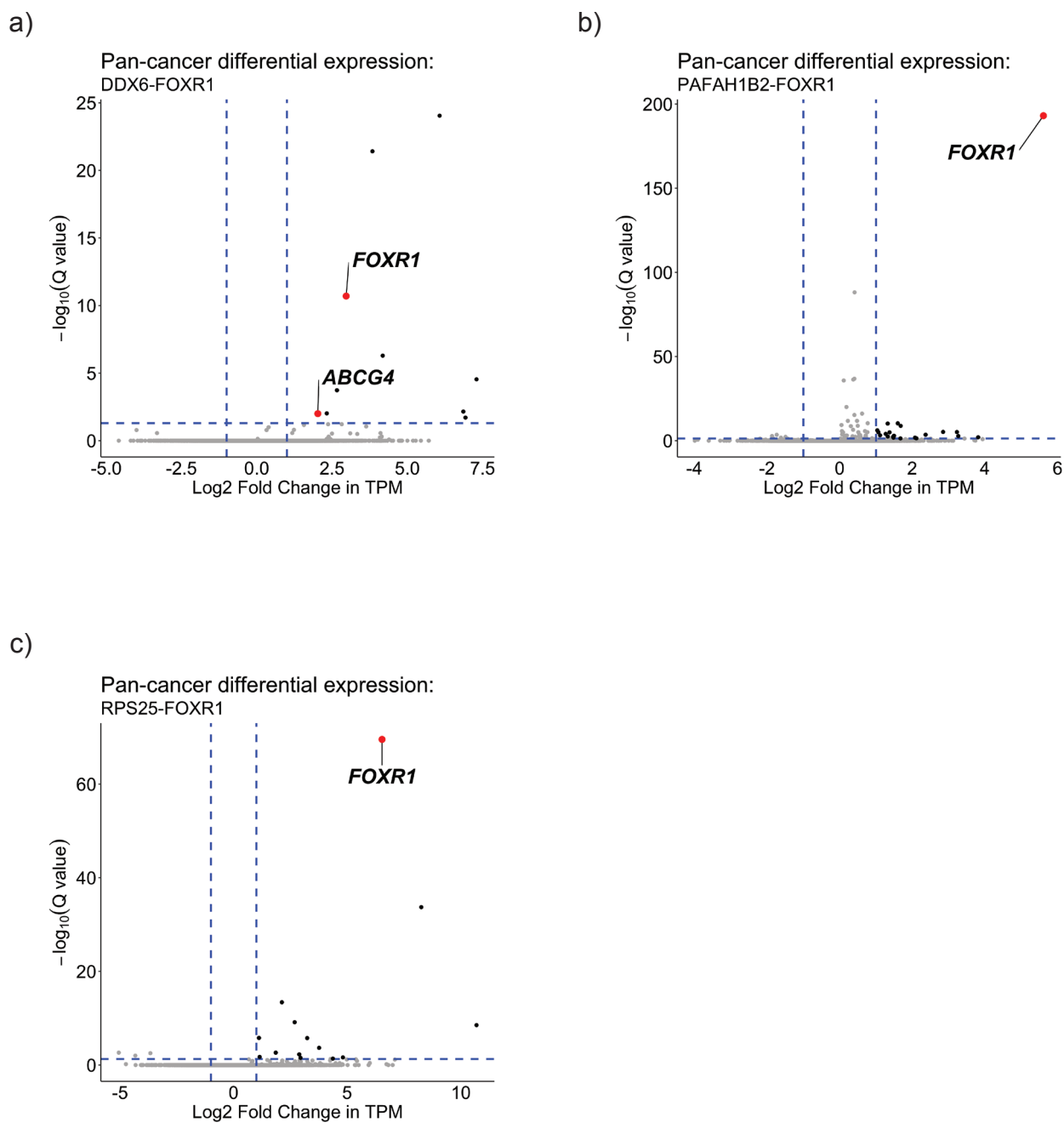
Supplementary Figure 13: Many COSMIC cancer census genes and kinases are found among fusion-associated dependencies. **a**, Left to right, stratified by COSMIC and non-COSMIC fusions with associated dependencies: proportion of fusions with associated dependencies that are COSMIC cancer census genes, proportion of fusions with partners that are COSMIC cancer census genes, proportion of fusions with associated dependencies that are kinases, proportion of fusions with partners that are kinases. **b**, Top: BCL2-IgH is seen and associated with BCL2 dependency in a B-ALL cell line, JM1. Bottom: JM1 has increased sensitivity (lower AUC) to BCL2 inhibitor venetoclax, in line with what is seen in other B-ALL cell lines ($p = .00014$, two-sided t-test for B-ALL cell lines vs all other cell lines). **c**, Fusion partners associated with copy number amplification, are associated with multiple other dependencies. Top: ERBB2-JUP is seen in an esophageal cancer cell line, OE33. Bottom: MDM2-IL22 is seen in a clear cell renal cell carcinoma cell line, UOK101.

Supplementary Figure 14



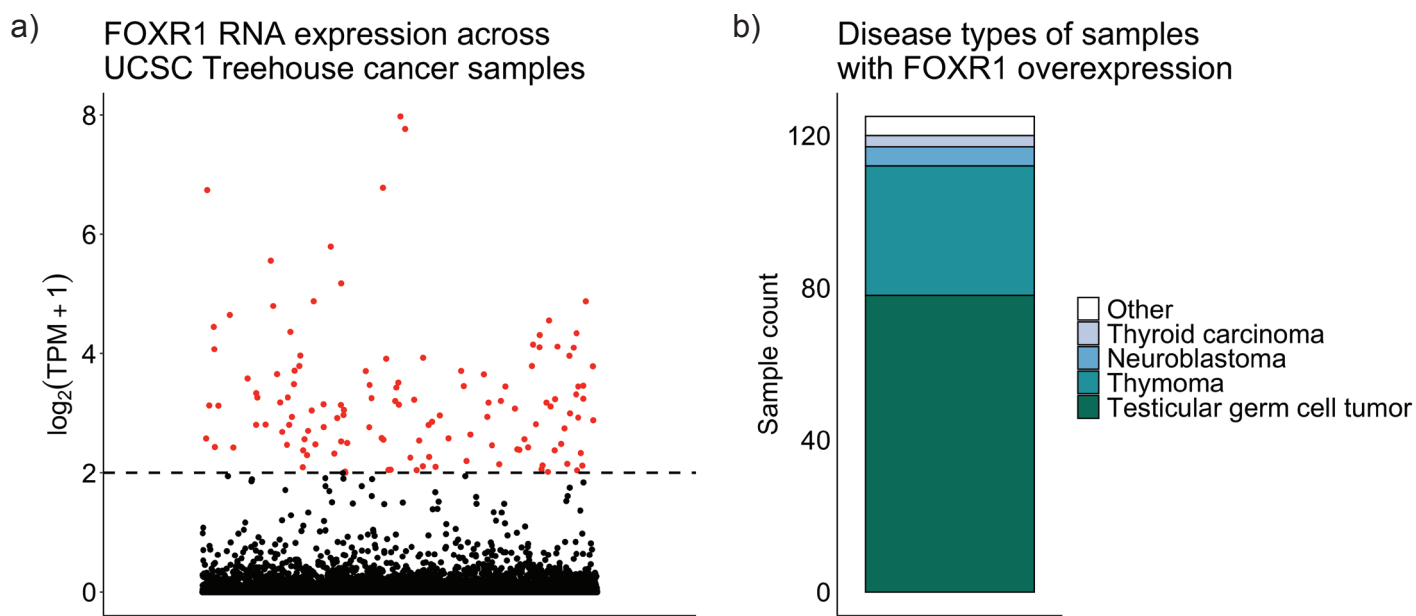
Supplementary Figure 14: Dependency data for other ERBB2 and MDM2 fusions. Fusion partners associated with copy number amplification, are associated with multiple other dependencies. a, ERBB2-CDK12 is seen in a gastric cancer cell line, NCIN87. **b,** ERBB2-CHMP4C is seen in a breast cancer cell line, HCC1419. **c,** MDM2-CAMKK2 is seen in a neuroblastoma cell line, NGP. **d,** MDM2-KITLG is seen in a liposarcoma cell line, LPS6.

Supplementary Figure 15



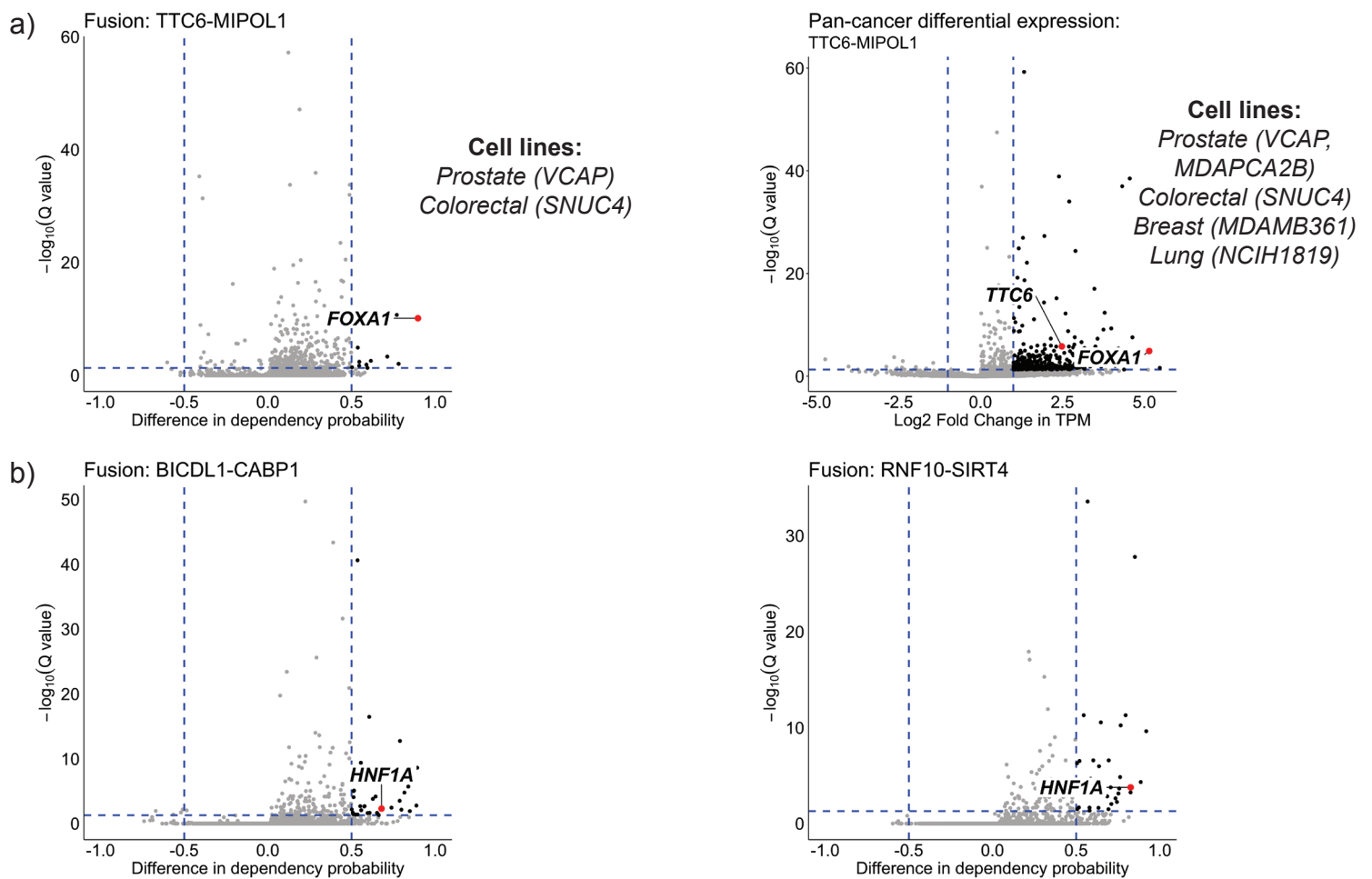
Supplementary Figure 15: FOXR1 expression in cell lines with FOXR1 fusions. FOXR1 fusions are associated with dependency on FOXR1 in three different cell lines. a, DDX6-FOXR1 is seen in bladder cancer cell line 639V. **b**, PAFAH1B2-FOXR1 is seen in osteosarcoma cell line 143B. **c**, RPS25-FOXR1 is seen in lung cancer cell line CALU6.

Supplementary Figure 16



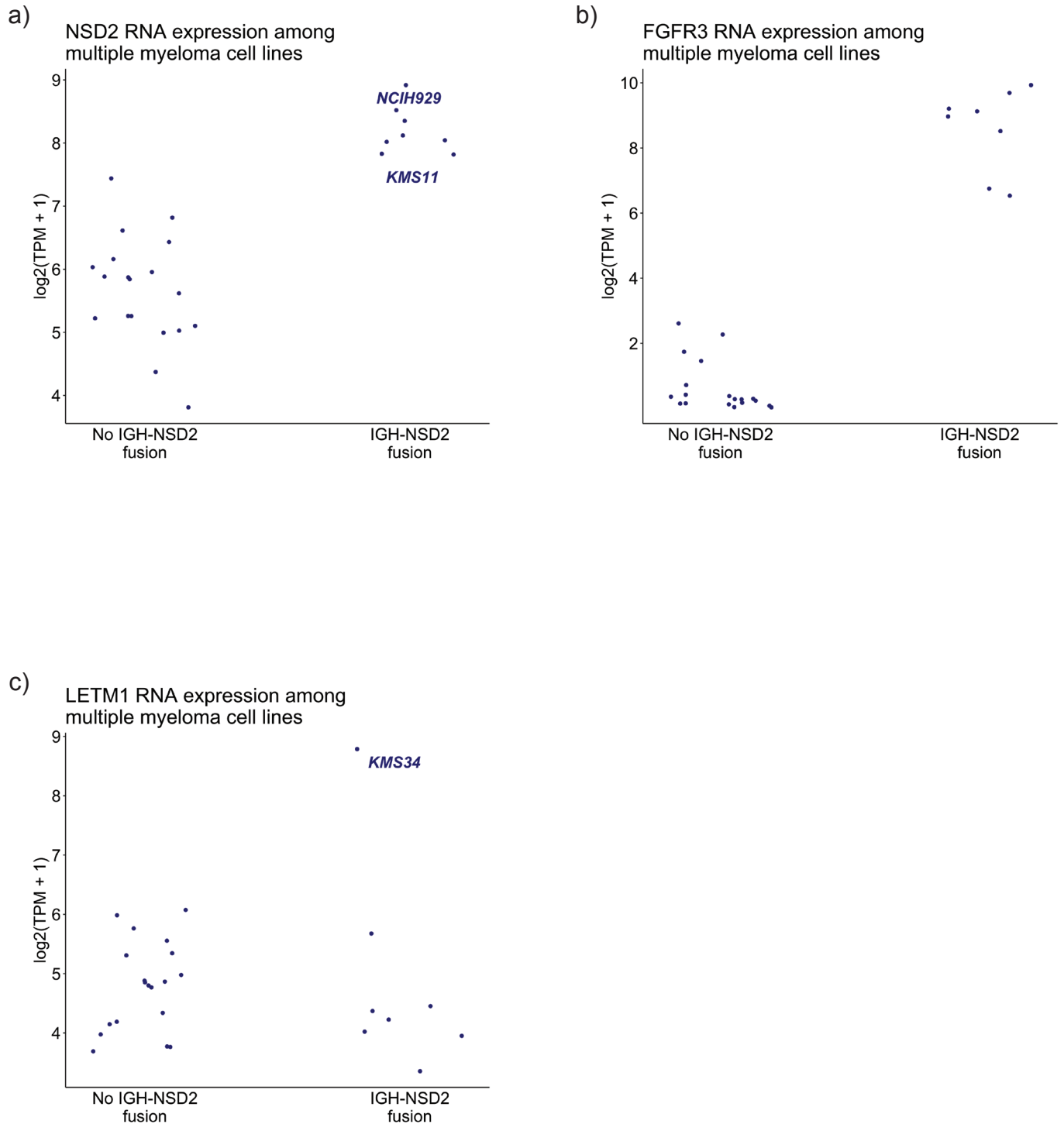
Supplementary Figure 16: FOXR1 expression in clinical samples. **a**, FOXR1 RNA expression across > 12,000 tumor samples across various histologies. **b**, Disease types of samples with FOXR1 overexpression.

Supplementary Figure 17



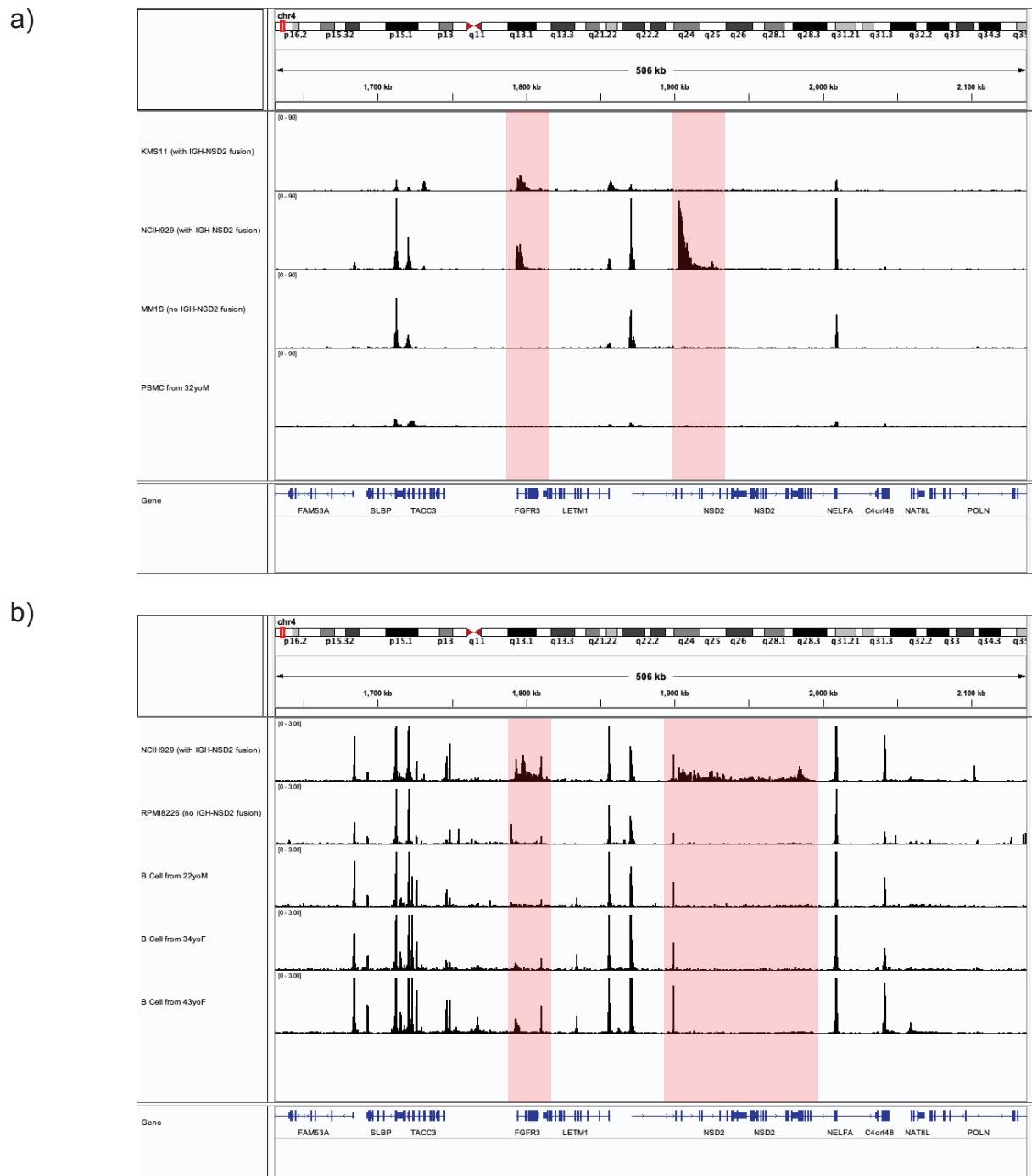
Supplementary Figure 17: Transcription factors are recurrent fusion-associated dependencies. a, FOXA1 is a dependency associated with the TTC6-MIPOL1 fusion. Left: Dependency space for TTC6-MIPOL1 in two cell lines demonstrating FOXA1 dependency. Right: Unbiased differential expression space for TTC6-MIPOL1 in five cell lines demonstrating FOXA1 overexpression. **b,** HNF1A is a collateral dependency in two separate gastric cancer cell lines, GSU and KE39.

Supplementary Figure 18



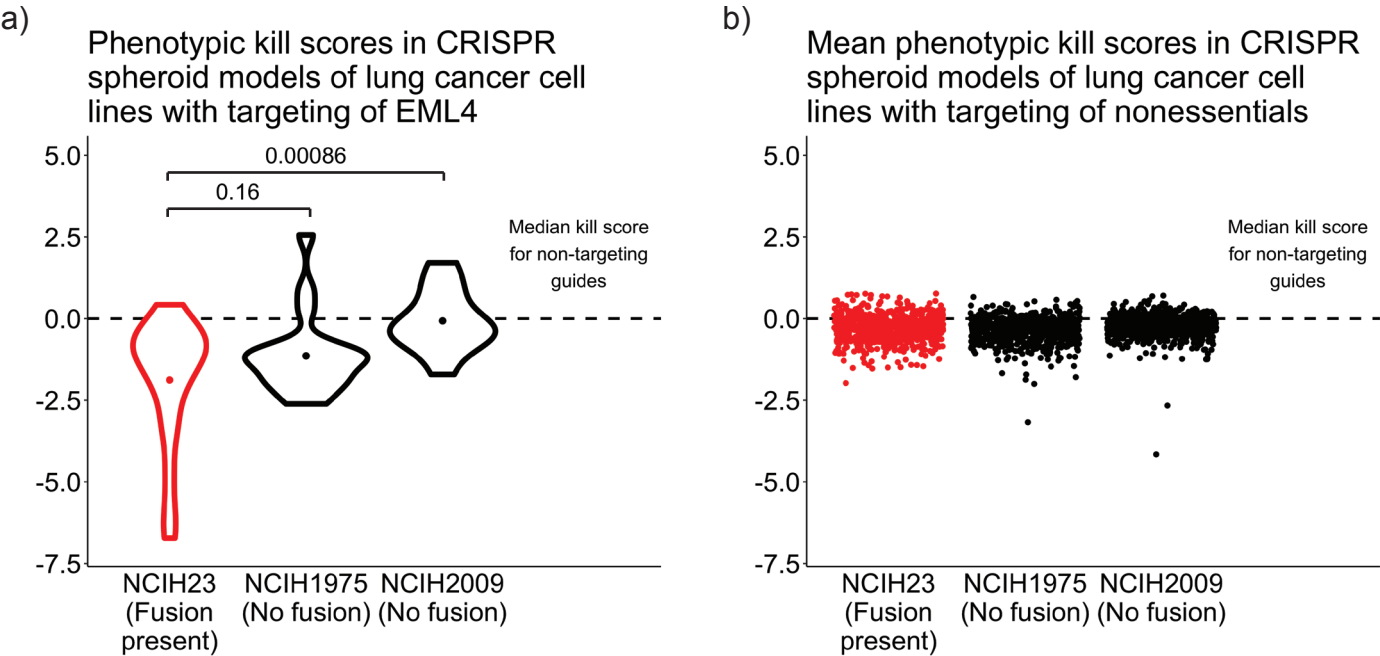
Supplementary Figure 18: RNA expression of NSD2 and LETM1 in IGH-NSD2 multiple myeloma. **a**, NSD2 expression in multiple myeloma cell lines stratified by the IGH-NSD2 fusion. Despite the increase in H3K27 acetylation at the NSD2 locus in NCIH929 relative to KMS11, the RNA expression of NSD2 is not significantly different between these two cell lines harboring the IGH-NSD2 fusion. **b**, FGFR3 expression in multiple myeloma cell lines stratified by the IGH-NSD2 fusion. FGFR3 is consistently overexpressed in cell lines with the IGH-NSD2 fusion. **c**, Expression of neighboring gene LETM1 in multiple myeloma cell lines stratified by the IGH-NSD2 fusion. The presence of the IGH-NSD2 fusion does not significantly impact the expression of LETM1, which is in close proximity to both NSD2 and FGFR3.

Supplementary Figure 19



Supplementary Figure 19: Epigenetic landscape of *FGFR3*, *NSD2*, and neighboring genes in IGH-*NSD2* multiple myeloma. **a**, H3K27 acetylation landscape of KMS11 (with IGH-*NSD2* fusion), NCIH929 (with IGH-*NSD2* fusion), MM1S (without IGH-*NSD2* fusion), and peripheral blood mononuclear cell lines. *FGFR3* is once again uniquely found to have increased H3K27 acetylation in NCIH929 in the setting of an IGH-*NSD2* fusion. In contrast to KMS11, H3K27 acetylation is increased at the *NSD2* locus in NCIH929. In NCIH929, there are other peaks of increased intensity visualized at *SLBP*, *TACC3*, the 5' region of *NSD2*, and *NELFA*; however, these are not consistently sustained in KMS11, suggesting no clear link between the epigenetic landscape of these genes and the IGH-*NSD2* fusion. **b**, DNase-seq landscape at NCIH929 (with IGH-*NSD2* fusion), RPMI8226 (without IGH-*NSD2* fusion), and B cells. Increased DNase-seq signal corresponding to a more open chromatin state is observed at *FGFR3* and *NSD2* in NCIH929 relative to RPMI8226 (a multiple myeloma cell line without the IGH-*NSD2* fusion) as well as several normal B cell samples. Other significant differences in DNase-seq at neighboring gene loci are not observed.

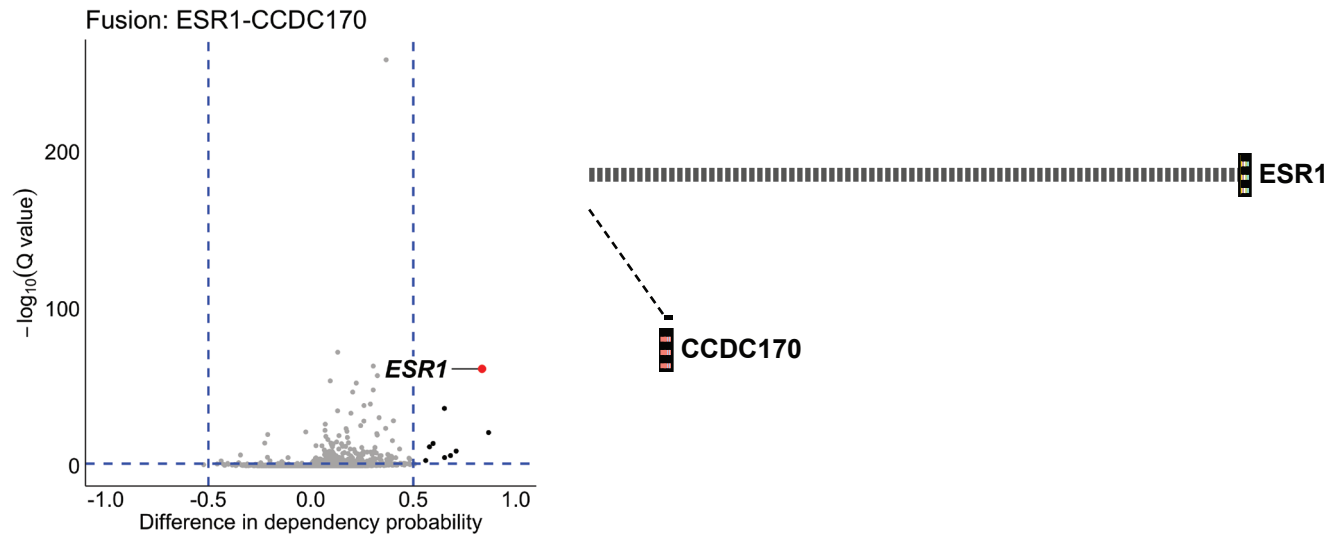
Supplementary Figure 20



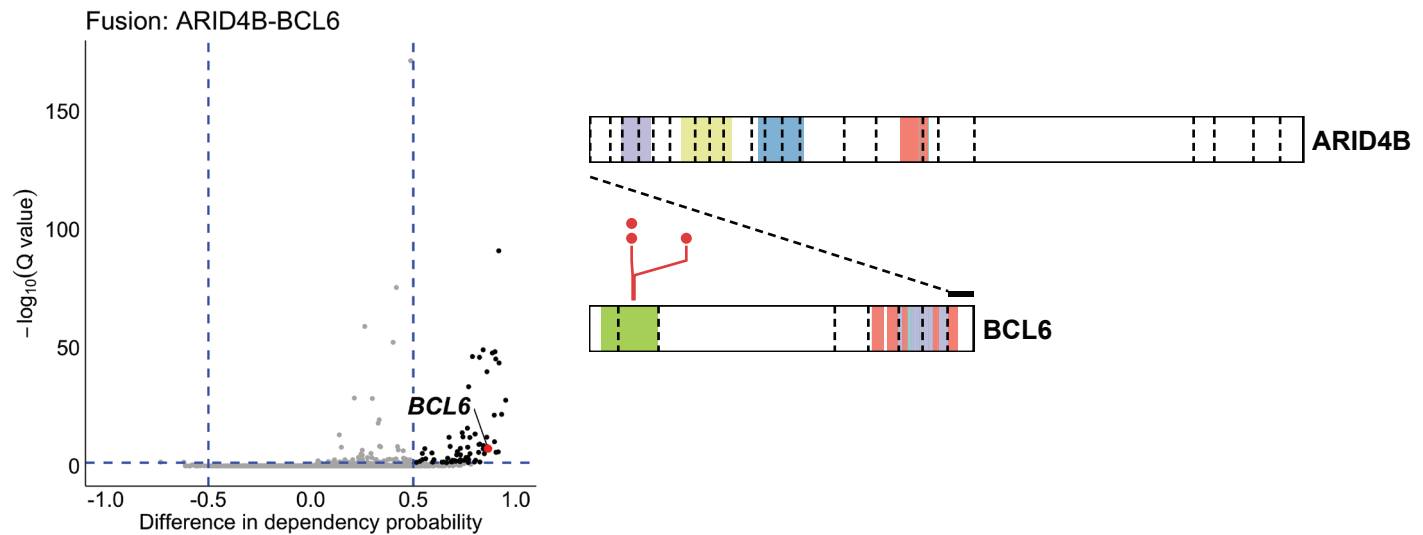
Supplementary Figure 20: Individual cancer spheroid model dependency data. Comparison of phenotypic kill scores of CRISPR sgRNAs in spheroid models derived from NCIH23 (with THADA-MTA3 fusion), NCIH1975 (without THADA-MTA3 fusion), and NCIH2009 (without THADA-MTA3 fusion). a, CRISPR sgRNAs targeting EML4 (point represents mean of each sgRNA distribution, p-values calculated by two-sided t-test). b, Mean of CRISPR sgRNAs targeting all nonessential genes (each point represents mean of sgRNA distribution for each nonessential gene).

Supplementary Figure 21

a)



b)



Supplementary Figure 21: Dependency data for select fusions where sgRNAs are located off the fusion transcript.

a, Dependency space for cell lines with ESR1-CCDC170 fusion. ESR1 screens as a dependency despite the fact that the ESR1-CCDC170 fusion transcript does not include the coding sequence of ESR1-CCDC170, and thus the sgRNAs (not pictured) are located off the ESR1-CCDC170 fusion transcript. **b**, Dependency space for cell lines with ARID4B-BCL6 fusion. BCL6 screens as a dependency despite the fact that the sgRNAs (red lines) are located off the ARID4B-BCL6 fusion transcript. Colored regions represent known functional domains.